

# Implication of the striped pulsar wind model for gamma-ray binaries

Jérôme Pétri<sup>1</sup> and Guillaume Dubus<sup>2</sup>

<sup>1</sup>*Observatoire Astronomique de Strasbourg, UMR 7550 Université de Strasbourg, CNRS, 11 rue de l'Université, 67000 Strasbourg, France*

<sup>2</sup>*UJF-Grenoble 1 / CNRS-INSU, Institut de Planétologie et d'Astrophysique de Grenoble (IPAG) UMR 5274, Grenoble, F-38041, France*

Accepted . Received ; in original form 7 November 2018

## ABSTRACT

Gamma-ray binaries are massive stars with compact object companions that are observed to emit most of their energy in the gamma-ray range. One of these binaries is known to contain a radio pulsar, PSR B1259-63. Synchrotron and inverse Compton emission from particles accelerated beyond the light cylinder in striped pulsar winds has been proposed to explain the X-ray to high energy (HE,  $> 100$  MeV) gamma-ray emission from isolated pulsars. This pulsar model extends naturally to binary environments, where seed photons for inverse Compton scattering are provided by the companion star. Here, we investigate the possibility of gamma-ray emission from PSR B1259-63 in the framework of the striped pulsar wind model. The orbital geometry of PSR B1259-63 is well constrained by observations and the double radio pulse suggests an almost orthogonal rotator so that the solid angle covered by the striped region is close to  $4\pi$ . We calculate the orbital and rotational phase-resolved spectral variability and light-curves to expect. We find that the recent detection by the *Fermi*/LAT of PSR B1259-63 close to periastron can be explained by a striped wind if the emission arises from a large range of radii ( $\geq 1000r_L$ ). We constrain the particle density number at the light-cylinder  $n_L \approx 7 \times 10^{15} \text{ m}^{-3}$ . The re-brightening a month after periastron passage could be due to interaction with additional seed photons from the trailing pulsar wind nebula. Striped winds may also be at work in the gamma-ray binaries LS I +61°303 and LS 5039, both of which have HE gamma-ray spectra reminiscent of those of pulsars and fluxes modulated on the orbital period. Gamma-ray pulsations are expected. Some gamma-ray binaries should be faint in HE gamma rays (HESS J0632+057) because the line-of-sight does not cross the striped wind region.

**Key words:** Pulsars: general - Radiation mechanisms: non-thermal - Gamma rays: theory - Stars: winds, outflows

## 1 INTRODUCTION

Pulsars are thought to be highly magnetized rotating neutron stars. Many of these pulsars, previously known as radio emitter, have now also firmly been detected in gamma rays (Abdo et al. 2010a). For some of them, the radiated energy is mainly released in the MeV/GeV range: there are called gamma-ray pulsars. Unprecedented access to this energy range is currently provided by the *Fermi Gamma-ray Space Telescope* Large Area Telescope. With more than fifty pulsars identified so far, and regular new identifications, compared to the handful previously known, the *Fermi*/LAT has made it possible to characterize the high energy phase-resolved spectra (HE,  $\gtrsim 100$  MeV) of a significant population of pulsars. These HE spectra are fitted by a hard power law, with photon index  $\Gamma$  between 1 and 2, supple-

mented by an exponential cut-off at energies claimed to lie between 1 and 5 GeV (Abdo et al. 2010a). Pulsed HE emission is usually explained by some radiation processes within the magnetosphere of the pulsar. However, the absence of a super-exponential cutoff and strong gamma-ray opacities argue against models in which the gamma-ray emission arises near the surface of the neutron star surface ('polar cap') (Harding 2009), favoring models in which the HE emission arises from curvature radiation of particles accelerated in the vacuum gaps of the outer part of the magnetosphere ('outer gap') (Cheng 2009).

Pulsed HE emission may also arise in the pulsar wind well beyond the surface of the light-cylinder (Kirk et al. 2002). 3D numerical modeling of pulsar magnetospheres in the force-free approximation show that pulse profiles are better reproduced if the emission is assumed to arise in current

sheets just outside of the light cylinder, along the separatrix (Bai & Spitkovsky 2010). The field structure beyond the light-cylinder, where the rotation of the neutron star requires that magnetic field lines open up, tends towards a split monopole configuration. The misalignment of the magnetic moment with respect to the rotation axis imprints a spiral wave shape to the underlying current sheet (Coroniti 1990; Michel 1994). The resulting *striped pulsar wind* expands radially at relativistic speeds with a period equal to that of the pulsar. Beamed emission from relativistically hot particles flowing in the current sheets, mostly in the first few stripes, leads to pulsed gamma-ray emission. In particular, this model has been successfully applied to reproduce observations of the phase-resolved optical polarization of the Crab pulsar (Pétri & Kirk 2005), phase-resolved spectra of Geminga and Vela (Pétri 2008, 2009) as well as light-curves of various *Fermi* pulsars (Pétri 2011).

Unlike in the outer gap models, the radiative process producing the HE gamma rays in the striped wind is not curvature radiation, which is negligible outside the light-cylinder, but inverse Compton (IC) scattering of ambient fields, typically the thermal X-ray emission from the neutron star itself, the cosmic microwave background or synchrotron self-Compton. Another possible source of seed photons, for pulsars in binaries, is light from the companion (let it be a second pulsar, a white dwarf, a low-mass or a massive star). The photon field orientation and density change as a function of orbital phase, affecting IC scattering in the stripes. This can lead to substantial variations in the pulsed gamma-ray spectra along the orbit, something which is not expected in standard magnetospheric models where the gamma-ray emission arises from curvature radiation and is thus a priori impervious to the external photon field.

In this paper the expected variation of pulsed gamma-ray emission with orbital phase is investigated using the specific case of PSR B1259-63, a 48 ms radio pulsar in a 3.4 year eccentric orbit around a  $10 M_{\odot}$  Be star (SS 2883). The system appears well-suited to test the model since the Be star has a high luminosity,  $L_{\star} \approx 10^{31}$  W, while the orbital separation  $d$  varies by more than a factor 10 between periastron ( $d \approx 0.7$  a.u.) and apastron ( $d \approx 9.5$  a.u.). Although pulsed emission from PSR B1259-63 has been detected in radio, only non-pulsed counterparts have been observed in X-rays and in very high energy gamma-rays (VHE,  $\gtrsim 100$  GeV) around periastron passage. This emission is attributed to radiation from particles accelerated at the termination shock of the pulsar wind. Striped pulsar wind emission would be expected to add another variable spectral component, peaking in HE gamma rays. Recently, HE emission has been detected using the *Fermi*/LAT (Abdo et al. 2011a; Tam et al. 2011). A first detection coincided with the passage of the source around periastron (mid-December 2011), where IC scattering from target photons of the companion star should be most efficient. The flux above 100 MeV is  $\approx 10^{-7}$  ph cm $^{-2}$ s $^{-1}$  with a power-law spectrum of photon index  $\approx 2$ . A second detection occurred after a lull of about a month. The flux was about 10 times higher than in mid-December and the spectrum was softer (photon index  $\approx 3.0$ ). No gamma-ray pulsation were detected.

The aim of this study is to investigate whether the HE gamma-ray detection of PSR B1259-63 can result from the orbital phase-dependence of pulsed HE emission from the

striped pulsar wind. The striped wind model and related assumptions are presented in §2. The specific application to PSR B1259-63 is described in §3. The relevance of our model to interpret the recent detections of PSR B1259-63 by *Fermi*/LAT and for other gamma-ray binary systems like LS 5039 and LS I +61°303 is discussed in §4 before concluding.

## 2 STRIPED PULSAR WIND MODEL

The assumptions of the striped pulsar wind model, as already discussed in several previous works (Kirk et al. 2002; Pétri & Kirk 2005; Pétri 2009, 2011) are briefly recapped in §2.1 and some specificities linked to the binary environment are explained in §2.2.

### 2.1 General assumptions about the wind

The rotation of the pulsar launches to first approximation a purely radially expanding wind, isotropic in space and carrying a  $e^{\pm}$ -pair density number falling off with distance to the center of the pulsar  $r$  faster than  $r^{-2}$  due to adiabatic cooling. These pairs are distributed according to a power law distribution function of index  $p$  with minimum and maximum Lorentz factor respectively  $\gamma_{\min}$  and  $\gamma_{\max}$  such that

$$dn = n(\gamma) d\gamma = K_e \gamma^{-p} d\gamma \quad (1)$$

with  $K_e$  given by Eq. (8) in Pétri (2009) with

$$K_e = \frac{(N - N_0)\text{sech}^2(\Delta\varphi\psi) + N_0}{r^2}. \quad (2)$$

This expression does not yet include adiabatic cooling because it falls off like  $r^{-2}$ . Nevertheless, adiabatic cooling can be accounted for by altering the radial power law dependence of the square of the distance  $r$  in the expression for the particle density number. Adding an extra radial dependence, assuming a non accelerating wind, we find a modified power law such that the density number decreases as  $r^{-2(p+2)/3}$ , the power law exponent depends on the exact motion of the wind, linear acceleration would lead to another exponent (Kirk et al. 2002). Here, the maximal energy  $\gamma_{\max} m_e c^2$  of the pairs (in the comoving frame) sets the location of the cutoff in the IC gamma-ray spectrum, an important observational constraint. We argue in §3.3 that the characteristic  $\gamma$  of this cutoff (or break) can be related to other parameters of the striped wind.  $N_0$  sets the background particle density number outside the current sheet whereas  $N$  represents the maximal density within the sheet. For more details, we refer to Pétri (2009).

The magnetic field geometry assumes a split monopole for which exact analytical solutions exist, see for instance Bogovalov (1999). The current sheet separating the two regions of opposite magnetic polarity remains small compared to the wavelength of the striped wind, with a finite thickness parameterized by the quantity  $\Delta\varphi$  (defined such that its value is high for a thin sheet). A smooth polarity reversal of the toroidal component of the magnetic field  $B_{\varphi}$  is enforced in this transition layer (Eq. (5)-(6) in Pétri 2009). Note that in the far asymptotic wind zone, the poloidal component of the magnetic field is negligible. We enforce it strictly to zero. Therefore, this asymptotic structure is a

simple Archimedean spiral with  $B_r = B_\theta = 0$  and  $B_\varphi \propto r^{-1}$ . The structure propagates radially outwards with a constant Lorentz factor  $\Gamma_v$  and the line-of-sight is inclined by an angle  $\zeta$  with respect to the neutron star rotation axis. The sheet wiggles around the rotational equatorial plane between angles  $+\chi$  and  $-\chi$ , where  $\chi$  is the obliquity of the pulsar, i.e. the angle between magnetic moment and rotation axis. Outside the current sheet, the plasma is cold but strongly magnetized whereas inside the sheet, it is hot and almost unmagnetized due to the zero magnetic field point (polarity reversal). The cold magnetized part has negligible thermal pressure.

The pairs in the current sheet emit synchrotron (X-rays) and IC (gamma-ray) radiation. Radiative cooling of the particles is not taken into account but the adiabatic one is. However, only the first stripes contribute significantly since the number density of particles decreases faster than  $r^{-2}$ . The emission is boosted by relativistic aberration when the wind expansion is directed towards the observer. Strong pulsed emission therefore requires that the line-of-sight cross the current sheet i.e. that  $|\pi/2 - \zeta| \leq \chi$ . In this special geometric configuration the current sheet crosses the line-of-sight twice per rotation of the neutron star, producing two pulses of boosted emission (or only one pulse in the less favorable case where  $|\pi/2 - \zeta| \approx \chi$ ). The peak-to-peak phase separation of the pulses is given by  $\arccos(\cot \chi \cot \zeta)$ , which is exactly  $180^\circ$  for a line of sight contained in the equatorial plane, independent of the obliquity. The width of the pulses depends on the bulk Lorentz factor of the wind  $\Gamma_v$  and on the current sheet thickness  $\Delta_\varphi$ . The amplitude of the pulses is set in part by the ratio of particle density inside and outside the current sheet. For a detailed discussion on the relation between geometry and pulse shape, see Pétri (2011).

The emission extends over a range of radii starting beyond the light-cylinder  $r_L \equiv cP/2\pi$  for a pulsar of period  $P$ . The pulses are computed by integrating the IC emissivity over the first few stripes, taking into account Doppler boosting, time retardation effects and adiabatic expansion.

The level of IC gamma-ray emission will also depend on the density of particles in the pulsar wind. The density is stronger in the striped wind region (angles between  $\pi/2$  and  $\pi/2 - \chi$  with respect to the vertical axis) because of the contrast  $N/N_0$  with the cold, strongly magnetized part of the wind. The maximum density for a given distance to the neutron star is at an angle  $\chi$ , along the crest of the current sheet wave. The width of this maximum is tied to the thinness of the current sheet  $\Delta_\varphi$ . All other things being equal, the strongest IC emission will occur when the line-of-sight passes through the edge of the striped wind, in the region spanned around a latitude  $\chi$ . A single pulse in HE gamma rays is expected for this particular pulsar orientation. A small amount of (unpulsed) IC emission may also be expected when the line-of-sight does not cross the striped wind because of the assumed small residual density of particles  $N_0/r^2$  away from the current sheet modulo adiabatic cooling. The emission will be unpulsed and the cold pairs will produce a sharp Compton line (Ball & Kirk 2000; Khangulyan et al. 2007; Cerutti et al. 2008) or broader band gamma-ray emission if the pairs are assumed to have power law distributions (Sierpowska & Bednarek 2005; Sierpowska-Bartosik & Torres 2007, 2008). Here, the energy

dissipation is limited to the striped part of the wind, entailing the geometrical constraints described above for HE gamma-ray observability.

## 2.2 Binary environment

In a binary, the orientation of the pulsar seen by the observer does not change along the orbit (except possibly on super-orbital timescales due to precession of the neutron star). Hence, synchrotron emission from the striped wind stays constant. However, IC emission from up-scattered stellar photons will change with orbital phase because the angle between the neutron star, the companion and the observer changes (Dubus et al. 2008). The calculation of the gamma-ray emission is changed from previous works to correctly follow the anisotropic scattering and to include relativistic aberration in the pulsar wind frame of this external source of seed photons. Useful analytical expressions can be derived for a power-law distribution of  $e^+e^-$  scattering off photons with a blackbody spectrum from a point source, both in the Thomson (Dubus et al. 2010) and Klein-Nishina regimes. Here we use approximate expressions for a mono energetic photon field as given by Moskalenko & Strong (2000) (see Appendix). Relativistic boosting effects due to the pulsar wind motion are taken into account by Lorentz transforming the particle distribution function (Eq. 1) from the comoving frame to the pulsar/observer frame, see Pétri (2009).

## 3 APPLICATION TO PSR B1259-63

In this paragraph, we first review the essential characteristics of the PSR B1259-63 system, then show spectral features expected from the striped wind model before closing with some estimates of the relevant parameters.

### 3.1 Description of the binary and pulsar

PSR B1259-63 / SS2883 is part of the small group of gamma-ray binaries, systems sharing a number of observational properties (notably a high level of HE or VHE gamma-ray emission compared to X-rays; Dubus 2006) and which have been conjectured to all harbor rotation-powered pulsars. Power-law spectra with exponential cutoffs and a flux varying on the orbital period have been observed in two other gamma-ray binaries, prompting speculations as to whether this could be accommodated by pulsar emission (see §4.2). PSR B1259-63 remains the only system of this group where a pulsar has been detected.

PSR B1259-63 is a 47.76 ms radio pulsar in a 1236.7 day orbit around a  $10 M_\odot$  and  $6 R_\odot$  Be star (SS 2883) with a temperature  $T_* \approx 27,000$  K (Johnston et al. 1994). The distance  $D$  to the system is about 1.5 kpc. The temperature and distance have been recently revised to 27,500–34,000 K and 2.3 kpc respectively (Negueruela et al. 2011). The orbit is eccentric with  $e = 0.87$  while the inclination of the system  $i$  is about  $36^\circ$ , which implies that the distance of the pulsar to the Be star varies from  $9.9 \times 10^{10}$  m (periastron, orbital phase  $\phi_{\text{orb}} = 0$ ) to  $1.4 \times 10^{12}$  m (apastron,  $\phi_{\text{orb}} = 0.5$ ) and that the angle between the Be star, pulsar and observer varies between  $\pi - i = 54^\circ$  (superior conjunction,  $\phi_{\text{orb}} \approx 0.995$ ) and  $\pi + i = 126^\circ$  (inferior conjunction,  $\phi_{\text{orb}} \approx 0.045$ ). Hence, the

stellar photon density seen by the pulsar increases by a factor 200 at periastron, compared to apastron, and this is also where the effects of anisotropic IC scattering should be most manifest. HESS observations have detected strongly phase-dependent VHE emission around periastron, interpreted as IC emission from pairs accelerated or randomized at the pulsar wind termination shock (Aharonian et al. 2005, 2009). The first periastron passage observable by the *Fermi*/LAT occurred in mid-December 2010 and has resulted in the detection of variable HE emission (see §1).

The measured pulse period derivative implies an energy loss rate for the pulsar of  $\dot{E} \approx 8 \cdot 10^{28}$  W and a magnetic field  $B \approx 3.3 \cdot 10^7$  T. The radio pulsations are eclipsed close to periastron by material in the circumstellar disk of the Be star (Melatos et al. 1995). The pulse profile is reminiscent of the Crab pulse profile, with two peaks of commensurate amplitude separated by  $145^\circ$  (Connors et al. 2002). Pulsations have not been detected in other wavelengths; the upper limit on the amplitude in X-rays is 2% (Chernyakova et al. 2006). Following Pétri (2011), radio pulsations are thought to arise close to the polar caps, which are visible to the observer only when  $\zeta \approx \chi$ . Furthermore, the double peaked radio pulse profile in PSR B1259-63 suggests a nearly orthogonal rotator, constraining the obliquity  $\chi \approx 90^\circ$ . In this case, the average density around the pulsar is only weakly dependent on latitude and pulsed HE emission is expected over most of the sky. The geometrical parameters of the striped wind model are therefore favorable and significant pulsed HE emission can be expected near periastron due to the increased seed photon density from the Be star.

### 3.2 Orbital dependence of the striped wind emission

From the model exposed in §2, we compute light-curves and spectra accounting only for photons from the companion, neglecting all other contributions. This will give a first insight into the orbital phase dependence of the pulse shape and phase-resolved spectra. When discussing the results below, a clear distinction must be kept between emission modulated by *orbital phase* due to the binarity of the system and modulation induced by the *rotation of the neutron star* and responsible for the pulsed emission.

As discussed above, we expect a nearly orthogonal rotator with the line-of-sight inclination close to  $90^\circ$ . More precisely, for the following plots, we choose  $\chi = 85^\circ$  and  $\zeta = 55^\circ$ . We take a mono-energetic photon field from the companion with an energy of 6 eV. The wind is mildly relativistic with  $\Gamma_v = 10$ . This value for the Lorentz factor seems relatively small but is motivated by the fact that a similar Lorentz factor ( $\Gamma_v \approx 20$ ) was already used to satisfactorily fit the phase-resolved optical polarization of the Crab pulsar (Pétri & Kirk 2005). Moreover, in our striped wind model, pulsed emission is assumed to be dominant very close to the light cylinder at the base of the relativistic outflow. This fact does not exclude the possibility of a bulk acceleration of the wind to much higher Lorentz factor, for instance due to magnetic reconnection in the stripes (Lyubarsky & Kirk 2001), while propagating towards the termination shock. The particle distribution function starts from  $\gamma_{\min} = 10^2$  up to  $\gamma_{\max} = 10^3$  with a power-law index  $p = 2$ . These values are justified in the discussion of §4.

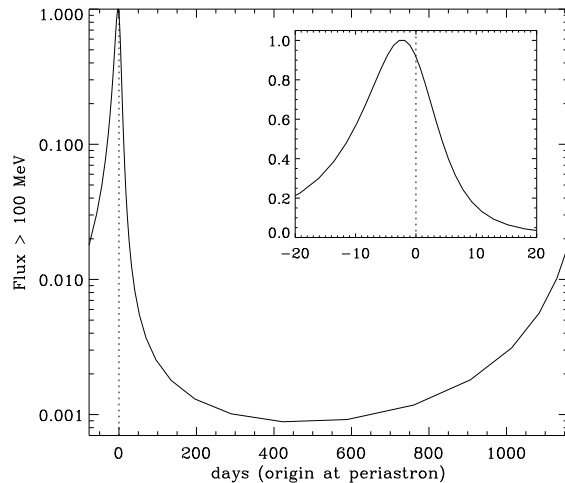


**Figure 1.** Lightcurve vs orbital phase for the pulse averaged high-energy emission from the striped wind above 100 MeV. The inset zooms in on periastron passage.

The orbital phase light-curve is shown in Fig. 1 for  $E > 100$  MeV. As expected, the flux peaks close to periastron passage (two days before). The contrast in flux is  $\approx 700$ , slightly more than the  $\approx 200$  contrast that would be derived from the seed photon density because of the angle dependence of inverse Compton scattering on a point source. Note the asymmetrical shape with a rising time longer than the falling time. Significant emission occurs on a short timescale, with the flux greater than 10% of its peak value from 28 days before periastron up to 13 days after periastron.

No variation of the pulse shape with orbital phase is expected because pulses are imprints of the current sheets that are independent of the scattering photon field, excepted for the peak intensity evolving with orbital phase according to Fig. 1. However, the shape is sensitive to the photon energy. This variation is quantified in Fig. 2 where we plot the pulsed light-curves against energy from X-rays ( $E \approx 1$  keV) to gamma-rays ( $E \approx 1$  GeV, assuming electrons are accelerated up these energies). At lowest energies, around a few keV, a non negligible off-pulse component remains visible between both pulses whereas at highest energies, above several MeV, pulses sharpen with decreasing width and vanishing off-pulse part. We emphasize that this trend is not correlated with any orbital motion, it is an intrinsic feature of the pulsed radiation mechanism invoked for pulsar, entirely produced by relativistic beaming effects, let it be isolated or in binaries. In the striped wind scenario, if beaming disappears so does pulsed emission. This trend in pulse variation is closely related to the Doppler boosting of the spectral flux density from the wind frame to the observer frame. Indeed the Lorentz factor shapes the pulse profiles. On one side, if the beaming remains to weak, the DC component dominates with pulsation hardly detectable. On the other side, for ultrarelativistic flows, the pulse profiles become independent of the Lorentz factor and reflect the characteristics of the stripes, i.e. width and particle density number. This dependence is explained as follows. Assuming for instance a spectral slope of index  $\alpha$  in intensity, the spectral flux density  $F_\nu \propto \nu^{-\alpha}$  will be magnified by a factor  $\mathcal{D}^{2+\alpha}$  where

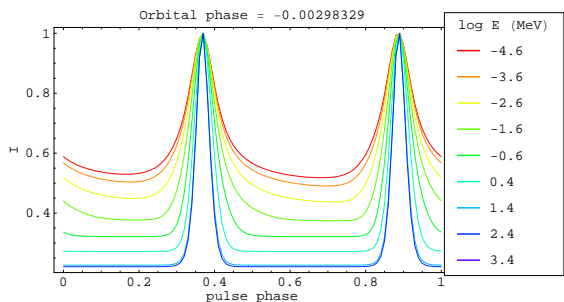


**Figure 2.** Variation of the pulsar light-curves as a function of energy for a given orbital phase, here we took  $\phi = -0.00298$ . A smooth change with increasing contrast in pulses is recognizable when moving from lower to higher energies. Peak intensities are normalized to unity.

$\mathcal{D} = 1/\Gamma_v(1 - \beta_v \cdot \mathbf{n})$  is the relativistic Doppler factor (see §3.3 below). The enhancement therefore strongly depends on this index  $\alpha$  thus on photon energy. Note that if PSR B1259-63 is an orthogonal rotator then the time lag between gamma-ray and radio pulses should correspond to  $P/4$ ,  $1/4$  of the pulsar period or  $90^\circ$  in phase, according to Eq. (31) in Pétri (2011).

An example of spectra for different orbital phases is plotted in Fig. 3. Three distinct parts corresponding to three different slopes are visible. First, the spectrum is hard ( $\alpha = 0$ ) below the low energy cut-off around a few 10 MeV implied by the minimum Lorentz factor of the particle power law distribution function. The beaming is  $\propto \mathcal{D}^2$ . The flux in X-ray (around 1 keV) is two to three orders of magnitude fainter than the gamma-ray flux. Most of the pulsed emission is radiated around 10 MeV. Second, between a few 10 MeV and a few GeV, the classical Thomson regime applies with a softer spectrum  $\alpha = (p - 1)/2$ , leading to more effective beaming  $\propto \mathcal{D}^{2+\alpha}$  and sharper pulses. Finally, the Klein-Nishina regime corresponding to the softest part of the spectrum, above a few GeV, the highest values of  $\alpha$  are reached, therefore a very effective beaming and strongly pronounced pulses.

The characteristic frequencies of the spectrum (associated with the minimum electron energy and the Klein-Nishina transition) change slightly with orbital phase because of the dependence of the inverse Compton cross-section with angle. The effect will be stronger for a more edge-on inclination of the binary orbit (see Fig. 1 in Dubus et al. (2008)).

### 3.3 Estimated striped wind luminosity

We have reviewed the basic assumptions behind the striped wind model and we have shown that it leads to orbital modulations. Here, we give some analytical estimates of the synchrotron and inverse Compton luminosity from the striped wind. The relevant quantities are the Lorentz factor  $\Gamma_v$ , the magnetic field  $B_L$  and the particle density number  $n_L$  within the sheet at the light-cylinder radius  $r_L$ . For PSR B1259-63,  $B_L$  is equal to 2.7 T at the light cylinder radius  $r_L = 2.3 \times 10^6$  m.  $\Gamma_v$  and  $n_L$  will be constrained from the observations.

Assuming pressure balance in the current sheet between

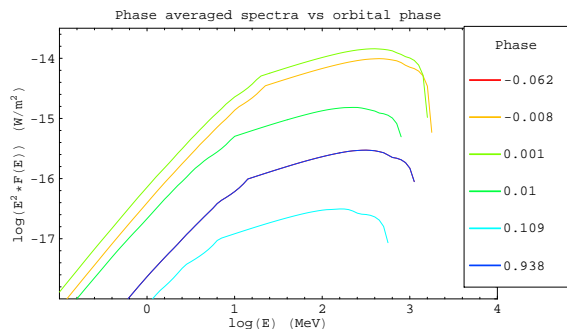


**Figure 3.** High-energy pulse averaged spectra of the striped wind for different orbital phases of the binary. The physical parameters are estimated according to the discussion in §3.3.

the particles and the magnetic field implies

$$\frac{1}{3} \gamma' n'_e m_e c^2 = \frac{B'^2}{2\mu_0} \quad (3)$$

where the  $\gamma'$  is the mean Lorentz factor of the pairs,  $n'_e$  is the particle density and  $B'$  the magnetic field. Primed quantities refer to values measured in the frame comoving with the wind and the subscript  $L$  refers to values at the light cylinder. Introducing the magnetization parameter defined as

$$\sigma \equiv \frac{B'^2}{\mu_0 n'_e m_e c^2} = \frac{B^2}{\mu_0 \Gamma_v n_e m_e c^2} = \frac{B_L^2}{\mu_0 \Gamma_v n_L m_e c^2} \quad (4)$$

we get  $\gamma' \approx 3\sigma/2$ . Note that although  $B'$  and  $n'_e$  vary with distance to the pulsar,  $\sigma$  is actually constant with radius so that  $\sigma = \sigma_L$ , its value at the light cylinder radius. Therefore, with these assumptions,  $\gamma'$  is also constant with radius.

#### 3.3.1 Synchrotron flux

The synchrotron emissivity in the comoving frame, assuming isotropic radiation, is

$$j'_s(\nu') = \frac{n'_e}{4\pi} \frac{4}{3} \sigma_T c \gamma'^2 \frac{B'^2}{2\mu_0} \delta(\nu' - \nu'_s) \quad (5)$$

assuming that the mono-energetic particles radiate only at their synchrotron peak (cut-off) frequency

$$\nu'_s = \frac{3}{4\pi} \gamma'^2 \frac{e B'}{m_e} = \frac{3}{4\pi} \left( \frac{3\sigma_L}{2} \right)^2 \frac{e B_L}{m_e \Gamma_v} \left( \frac{r_L}{r} \right) \equiv \nu'_L \left( \frac{r_L}{r} \right) \quad (6)$$

where we have used that the magnetic field is purely toroidal. The synchrotron flux measured by a distant observer located at distance  $D$  is

$$F_s(\nu) = \frac{1}{D^2} \int j_s(\nu) dV = \frac{1}{D^2} \int \mathcal{D}^2 j'_s(\nu') dV \quad (7)$$

Recall that only the stripes radiate significantly. Thus the effective volume is much less than the total volume occupied by the wind, the ratio between both is symbolized by  $\Delta$  which is around 0.1 and  $dV = \Delta r^2 dr d\Omega$  (note that  $\Delta$  is different - but related to -  $\Delta_\varphi$ ). Integrating the above using the radial dependence of the synchrotron frequency (Eq. 6)

leads to

$$F_s(\nu) = \frac{2}{9D^2} \sigma_T n_L B_L r_L^3 \frac{m_e c}{\mu_0 e} \int_{\Omega_p} \frac{\mathcal{D}^2}{\Gamma_v^2} \Delta d\Omega \quad (8)$$

$$= \frac{8\pi}{9D^2} \sigma_T n_L B_L r_L^3 \frac{m_e c}{\mu_0 e} \frac{f_p \Delta}{\Gamma_v^2} \quad (9)$$

$$\approx 4 \times 10^{-45} \Delta n_L \Gamma_v^{-2} \text{ W m}^{-2} \text{ Hz}^{-1}. \quad (10)$$

where  $f_p$  is a coefficient of order unity due to the integration over the finite solid angle covered by the striped wind  $\Omega_p$ , usually less than  $4\pi$  steradians, and which we collate with  $\Delta$ . For a more general discussion including a power-law distribution of particle instead of a mono-energetic one, see Kirk et al. (2002).

### 3.3.2 Inverse Compton flux

The inverse Compton emissivity can be approximately calculated using a similar approach and assuming the Thomson regime (the validity of this assumption can be verified a posteriori). If the source of seed photons (star) is a point-like ( $R_* \ll d_*$ ) blackbody of temperature  $T_*$ , the comoving radiation density of seed photons is given by

$$u'_* = \Gamma_v^2 (1 - \beta_v \cos \theta_*)^2 \frac{\sigma_{\text{SB}} T_*^4}{c} \left( \frac{R_*}{d_*} \right)^2 \approx 0.5 \Gamma_v^2 \text{ J m}^{-3} \quad (11)$$

at periastron. Here,  $\theta_*$  is the angle between the direction of the star and the direction of motion of the electron. The dominant emission comes from those electrons that travel towards the observer. Hence, the angle varies between  $54^\circ$  and  $126^\circ$  (see §3.1) and  $(1 - \beta_v \cos \theta_*) \approx 1$ . In the following, we assume that the stellar radiation is isotropic in the observer frame. The striped wind emission is again assumed to be monochromatic at the frequency

$$\nu'_c = \frac{4}{3} \gamma'^2 \nu'_* \approx \frac{4}{3} \gamma'^2 \Gamma_v \nu_* = 3 \Gamma_v \sigma_L^2 \nu_* \quad (12)$$

where  $h\nu_* \approx 2.7kT_*$  is the peak frequency of the stellar blackbody in  $\nu F_\nu$ . The characteristic inverse Compton frequency is independent of radius so the high energy emission is a line at the rest frame frequency  $\nu_c = 3D\Gamma_v \sigma_L^2 \nu_* \approx 35 \Gamma_v^2 \sigma_L^2 \text{ eV}$  with a spectral flux

$$\nu_c F_c = \frac{1}{D^2} \iint \mathcal{D}^2 \frac{n'_e}{4\pi} \frac{4}{3} \sigma_T c \gamma'^2 u'_* \delta(\nu' - \nu'_c) \Delta dV d\nu \quad (13)$$

After integration, expressing the luminosity as a function of  $\Gamma_v$  and  $n_L$  gives

$$\nu_c F_c \approx \frac{3}{D^2} n_L \sigma_T c (\Gamma_v \sigma_L)^2 u_* r_L^2 l_{\text{em}} \Delta \quad (14)$$

$$\approx 1.2 \times 10^{-20} \Gamma_v \sigma_L \Delta \frac{l_{\text{em}}}{r_L} \text{ W m}^{-2} \quad (15)$$

where  $l_{\text{em}}$  is the range of radii over which there is emission, set in practice by particle cooling. In the above expression we have collated with  $\Delta$  the geometrical term

$$g_p = \frac{1}{4\pi \Gamma_v} \int_{\Omega_p} \mathcal{D}^3 d\Omega \approx 1 \quad (16)$$

that appears in the integration and which is of order unity. Note that  $g_p = 1$  only when the striped wind covers the full  $4\pi$  steradians. The inverse Compton luminosity depends on the orbital phase through the stellar radiation density (the numerical value given here is for periastron).

### 3.3.3 Striped wind parameters in PSR B1259-63

The expressions above are used to constrain the parameters of the striped wind in PSR B1259-63. The spectrum of PSR B1259-63 does not have a high enough S/N to constrain the presence of an exponential cutoff during the first detection in December (Abdo et al. 2011a), when the present model is thought to apply (see §4). Tam et al. (2011) report no detection above 1.4 GeV in the first detection and a spectral exponential cutoff around 300 MeV during the January 2011 flare. LS 5039 and LS I +61°303 show exponential cutoffs at a few GeV, in the range of the HE cutoffs (or breaks) observed in pulsars. Radiative or adiabatic losses or a complex distributions of pairs will readily widen the mono-energetic line in the simple approximation to power-law emission with a sharp cutoff, as observed in pulsars. We tentatively associate the inverse Compton frequency  $\nu_c$  derived above with an emission cutoff at a few GeV, typical of the observed *Fermi*/LAT pulsars (Abdo et al. 2010a), so that

$$h\nu_c = 3D\Gamma_v \sigma_L^2 h\nu_* \approx 3 \text{ GeV}. \quad (17)$$

This implies

$$\Gamma_v \sigma_L = \frac{B_L^2}{\mu_0 n_L m c^2} \approx 10^4 \quad \text{and} \quad n_L \approx 7 \times 10^{15} \text{ m}^{-3}. \quad (18)$$

The Lorentz factor of the electrons is  $\gamma = 3\sigma_L D/2 \approx 10^4$  so inverse Compton scattering on stellar photons of typical energy  $\epsilon_* = 2.7kT_* \approx 6 \text{ eV}$  is indeed in the Thomson regime. We are effectively setting  $\gamma_{\text{max}} = 10^4$  (in the observer frame). As an aside, the value of  $n_L$  puts a limit on the pair multiplicity factor  $\kappa$  in the polar caps. The Goldreich-Julian particle flux from both polar caps is

$$2\dot{N}_{\text{GJ}} \approx 4\pi \frac{\epsilon_0 \Omega^2 B_{\text{ns}} R_{\text{ns}}^3}{e} \approx 4 \times 10^{32} \text{ s}^{-1} \quad (19)$$

so the expected pair density at the light cylinder is

$$n_L \approx \kappa \frac{2\dot{N}_{\text{GJ}}}{4\pi r_L^2 c} \approx 2 \times 10^{10} \kappa \text{ m}^{-3} \quad (20)$$

and the pair multiplicity is constrained to

$$\kappa \approx 3 \times 10^5 \Delta^{-1}. \quad (21)$$

A comparable constraint for PSR B1259-63,  $\kappa \lesssim 8 \times 10^4$ , was derived by Pétri & Lyubarsky (2007) from considerations about magnetic dissipation at the termination shock.

The inverse Compton luminosity at periastron directly depends on the adopted spectral cutoff (Eq. 14), giving

$$\nu_c F_c(3 \text{ GeV}) \approx 1.2 \times 10^{-16} \Delta \left( \frac{l_{\text{em}}}{r_L} \right) \text{ W m}^{-2} \quad (22)$$

or  $4 \times 10^{24} \text{ W}$ , isotropic equivalent, to compare to a pulsar spindown power of  $8 \times 10^{28} \text{ W}$ . A significant fraction of the power is radiated in gamma rays only if a very large range of radii ( $l_{\text{em}}$ ) are involved. At periastron, the pulsar is at a distance from the star equivalent to  $4 \times 10^4 r_L$ . Hence, a large fraction of the pulsar power can in principle be radiated in gamma rays if the striped wind propagates most of the way to the star. Both particle cooling in the pulsar wind and ram pressure from the stellar wind will act to lower the actual level of high energy emission. The gamma-ray luminosity of PSR B1259-63 at periastron represents about 5% of the spindown power, so  $r_0 \approx 1000 r_L \Delta^{-1}$  in order to match the

observed flux. Note that the emission from each pulse is spread over a time  $l_{\text{em}}/\Gamma_v^2 c$ . The HE emission will remain pulsed only if  $l_{\text{em}} \leq \Gamma_v^2 r_L$  (Kirk et al. 2002), which requires  $\Gamma_v \geq 30\Delta^{-1/2}$ .

The synchrotron spectrum is a power-law with  $\nu F_\nu \propto \nu$ . The synchrotron frequency is no higher than its value at the light cylinder (Eq. 6) and presumably less if emission starts away from the light cylinder. At the light cylinder,

$$\nu_L \approx 2.5 \times 10^{11} \sigma_L^2 \text{ Hz}, \quad (23)$$

hence, the maximum synchrotron spectral luminosity is (Eq. 8)

$$\nu_s F_s(r = r_L) \approx 7 \times 10^{-18} \sigma_L^2 \Gamma_v^{-2} \Delta \text{ W m}^{-2} \quad (24)$$

This must be smaller than the spindown luminosity of the pulsar  $\approx 3 \times 10^{-12} \text{ W m}^{-2}$  at  $D = 1.5 \text{ kpc}$ , which yields the conservative limits  $\sigma_L \leq 650 \Gamma_v \Delta^{-1/2}$  and  $\nu_L \leq 10^{17} \Gamma_v^2 \Delta^{-1} \text{ Hz}$ . In the above we have fixed the characteristic gamma-ray energy to 3 GeV, imposing  $\Gamma_v \sigma_L \approx 10^4$ . Therefore, the synchrotron luminosity is no larger than  $\nu_s F_s \approx 7 \times 10^{-10} \Gamma_v^{-4} \Delta \text{ W m}^{-2}$ . The limit on spindown luminosity gives  $\Gamma_v \geq 4\Delta^{1/4}$  and  $h\nu_L \leq 10\Delta^{-1/2} \text{ keV}$ . A moderate Lorentz factor for the wind is enough to significantly reduce the synchrotron luminosity. This is consistent with the lack of a very hard component in the spectral energy distribution and with the non-detection of X-ray pulsations. The synchrotron flux is indeed very sensitive to the Lorentz factor of the wind Eq. (8). Much higher value than those adopted in this work would imply an undetectable synchrotron X-ray flux.

Taking into account the distribution in energy of pairs and cooling will spread the emission over a broader band. For instance, Thomson cooling of a mono-energetic pair injection results in a  $p = 2$  distribution for the pairs and  $\nu F_\nu \propto \nu^{1/2}$ . Pairs with  $\gamma \approx 10^4$  have an inverse Compton cooling timescale  $\approx 600 \text{ s}$  at periastron so adiabatic cooling probably dominates over radiative cooling. Adiabatic cooling of mono-energetic pairs gives a  $p = 1$  distribution and  $\nu F_\nu \propto \nu$ . The spectrum also has this slope below  $\gamma_{\text{min}}$  if the injection is a power-law (Fig. 4). The pulsed inverse Compton spectral luminosity in X-rays at 3 keV is thus expected to be from  $10^3$  to  $10^6$  times lower than at 3 GeV, consistent with the current upper limit on the X-ray pulsed fraction, 2% of  $2 \times 10^{-14} \text{ W m}^{-2}$  (Chernyakova et al. 2006).

## 4 DISCUSSION

The striped wind model in the environment of a massive star naturally leads to orbitally-modulated inverse Compton emission in the GeV range. The model involves several parameters, some attributed to the pulsar wind, like  $(\chi, \Gamma_v, N, N_0, \Delta\varphi)$ , supplemented with a prescribed particle distribution function, and some attributed to the binarity of the system, like star temperature, radius, orbit inclination angle, eccentricity, periastron position and photon density number, respectively  $(T_\star, R_\star, e, \omega, n_{\text{ph}})$ . As shown in the previous section, the pulsar wind parameters influence the observability of high energy emission, since pulsed emission from the striped wind can be detected only if the line-of-sight crosses the stripes, and the shape of this pulsed emission (Pétri 2011). The binary parameters influence the shape of the orbital modulation (Dubus et al. 2008).

### 4.1 *Fermi*/LAT detections of PSR B1259-63

The orbital parameters are relatively well known in PSR B1259-63. Pulsed emission from the striped wind can be detected only if the line-of-sight crosses the stripes. PSR B1259-63 is close to an orthogonal rotator owing to its double radio-pulse structure separated by roughly half a period (possible only if both magnetic poles are visible). As a consequence, stripes should fill the whole sky and high energy emission can be detected. Maximum inverse Compton flux is expected near periastron. We showed that, assuming the high energy emission cuts off at a few GeV like in pulsars or other gamma-ray binaries, the level of synchrotron and inverse Compton emission can be derived and is consistent with observations at periastron. We propose that the initial detection of gamma-ray emission from PSR B1259-63 is due to emission from the striped pulsar wind.

Curiously, much stronger HE emission was reported about a month after periastron passage. The reported flux level  $\approx 1.5 \times 10^{-6} \text{ ph cm}^{-2} \text{ s}^{-1}$  is 10 times higher than during the first passage, corresponding to a large fraction of the spindown luminosity (Abdo et al. 2011a; Tam et al. 2011). Although a high gamma-ray luminosity is possible (§3.3.3), this is not expected to occur after periastron passage since both the stellar radiation density is decreasing with distance and the geometry for inverse Compton scattering with stellar photons becomes less favorable (increasing interaction angle). The increase could be unrelated to the striped wind. If it is, additional contributions to the seed photon field could be involved.

For instance, the surrounding pulsar wind nebula (PWN) beyond the termination shock can contribute to the source of target photons. In binaries, the termination shock has a cone-like appearance, pointing more or less away from the star (Dubus et al. 2010), whose opening angle depends on the ratio of momentum fluxes from the stellar and pulsar winds (Bogovalov et al. 2008). The PWN emits mostly X-rays and gamma-rays with a luminosity bounded by the spindown luminosity, which is about 100 times lower than the luminosity of the Be star. The termination shock is typically expected to be closer than the star by a factor 10 (e.g. Tavani & Arons 1997; Dubus 2006), compensating the luminosity, but the interactions are less efficient as they occur in the Klein-Nishina regime. However, after periastron, the orbital geometry is such that the pulsar gradually moves in between the star and the observer. Hence, the cone moves in between the pulsar and the observer. If the cone has a large opening angle, pairs moving along the line-of-sight then encounter PWN photons with a progressively smaller interaction angle (closer to head on) than at periastron, while the angle with stellar photons increases (from  $54^\circ$  at superior conjunction, a week before periastron passage, to  $126^\circ$  at inferior conjunction, 55 days after periastron passage). As with external Compton emission in the relativistic jets of AGNs, the emission will be highly anisotropic. Doppler boosting of the PWN radiation density seen by the pairs moving towards the observer (in the direction of the PWN) and the increased upscattering rate along the line-of-sight can result in a much stronger gamma-ray flux. The steeper spectrum reported for the second detection could be due to the scattering occurring in the Klein-Nishina regime.

For completeness, we also note that emission from the

Be disk (van Soelen & Meintjes 2011) or thermal emission from the neutron star could also contribute significantly to the seed photon radiation density (although the scattering geometry is unfavorable in the latter case). We defer to future work an investigation of these processes and their relevance to explain the HE gamma-ray lightcurve after periastron passage.

#### 4.2 Evidence for a striped wind in other gamma-ray binaries

Two binaries, LS 5039 and LS I +61°303, are established HE gamma-ray sources (Abdo et al. 2009a,b) and have been conjectured to host pulsars with a large spindown power like PSR B1259-63 (Dubus 2006). *Fermi*/LAT observations showed that the HE gamma-ray emission does not connect naturally to the VHE emission detected by ground based Cherenkov arrays above 100 GeV. In both cases, there is an exponential cutoff at a few GeV, typical of the HE spectra of a gamma-ray pulsar. The HE emission appears to be due to a different population of particles than in VHE regime because of this cutoff. A straightforward solution is to interpret the HE as emission coming from the vicinity of the pulsar and the radio/X-ray/VHE as PWN emission arising beyond the termination shock.

*Fermi*/LAT observations showed that the HE gamma-ray flux from LS 5039 and LS I +61°303 is modulated on the orbital period, which would be difficult to explain via the usual magnetospheric emission processes (Abdo et al. 2009b) but is readily explained by the striped wind model developed in the previous sections. The HE gamma-ray emission should be pulsed but this is difficult to verify in a binary without an ephemeris for the pulsation.

The conditions are very similar to PSR B1259-63 except for the smaller orbits. The radiation density at periastron is greater by a factor  $\approx 50 - 1000$  and this implies a larger high gamma-ray luminosity. Indeed, the mean flux above 100 MeV is  $\approx 10^{-6}$  ph cm $^{-2}$  s $^{-1}$ . The orbital modulations are consistent with expectations from anisotropic inverse Compton scattering (Abdo et al. 2009a,b), which also apply to the striped wind model as discussed in the previous sections.

Interestingly, the HE lightcurve of LS I +61°303 peaks slightly later than expected, like PSR B1259-63. As discussed above, this might be explained if there is an additional source of seed photons besides the star, notably the PWN. Changes in the source of seed photons would also need to be invoked to explain the long term or orbit-to-orbit variability in the GeV lightcurve of LS I +61°303. Long term variability could also be attributed to pulsar precession. Such free precession has indeed been observed in pulsars like for PSR B1828-11 (Stairs et al. 2000) for which timescales of several months have been reported. Precession implies changes in the orientation of the striped wind with respect to the orbital plane, inducing a change in the particle density number along the line of sight.

A favorable orientation of the pulsar is required to invoke striped wind emission, implying the number of gamma-ray binaries may actually be greater than currently detected. If the distribution of obliquities is isotropic then a random line-of-sight crosses the striped wind in half of the pulsars. The model predicts a population of sources with

strong PWN emission (less susceptible to orientation issues) but weak or absent HE gamma-ray emission. Such systems would be most easily detected through their VHE gamma-ray emission by ground-based Cherenkov arrays. An example could be HESS J0632+057, a system very strongly suspected to be a gamma-ray binary (Hinton et al. 2009) but that has not been detected yet by the *Fermi*/LAT.

Finally, another important issue is the exact composition of the wind. Whereas a supply of electron/positron is easily achieved by pair creation in the polar caps, yielding a high multiplicity factor, the only possible source for ions would be from the stellar crust itself. We emphasize that despite the much lower density of ions, they can drastically affect the dynamics of the striped wind because of the large separation of time and spatial scales induced by the large mass ratio between leptons and ions. Indeed, the growth rates of some instabilities can significantly deviate from a pure electron/positron plasma and perturb the dissipation of magnetic field lines within the stripes, modifying the efficiency of the bulk acceleration of the wind. However, there is so far no clear evidence for such an ion component. The possible presence of ions in the striped wind has to be distinguished from the hadronic interpretation of the TeV light-curves expected from the *shocked wind*. In the latter, interaction of the pulsar wind with the companion star disk material could lead to significant emission but this emission would be unpulsed.

## 5 CONCLUSION

We have investigated the implications of the striped pulsar wind model in the context of gamma-ray binaries. Inverse Compton upscattering of stellar photons from the companion by pairs in the stripes generates high energy gamma-ray radiation that can be detected if the line-of-sight crosses the striped region of the wind (§2). The gamma-ray emission is expected to be pulsed and is also modulated along the orbit because of the changing photon density and scattering interaction angle (§3).

The weak HE gamma-ray emission from PSR B1259-63 detected near periastron can be explained by striped wind emission. The radio pulsations suggest PSR B1259-63 is an orthogonal rotator so that the line-of-sight always crosses the stripes. The inverse Compton emission is maximum close to periastron. The energy of the pairs is constant with distance from the pulsar if pressure balance between pairs and magnetic field is assumed in the stripes and cooling is neglected. Hence, a characteristic inverse Compton energy is expected that we associate with a spectral cutoff at a few GeV, by analogy with the spectra observed in the gamma-ray binaries LS 5039 and LS I +61°303. The level of synchrotron and inverse Compton flux depends on the wind Lorentz factor  $\Gamma_v$ , the magnetization  $\sigma_L$  and the volume occupied by the stripes. We find that a few % of the spindown luminosity can be radiated in gamma-rays if the emission occurs over a large range of radii (§3).

The gamma-ray emission should show a double-peaked pulsation at the rotation period of the neutron star with the pulse shape providing further diagnostics. Abdo et al. (2011a) searched for the pulsation but did not detect it (although, as they point out, PSR B1259-63 is well within the



range of  $\dot{E}$  and  $B_L$  where pulsed gamma-ray emission is typically detected from pulsars by the *Fermi*/LAT). Detecting the gamma-ray pulsation in this binary may be difficult to achieve because of the weak flux and variations in timing solution around periastron (Wang et al. 2004). Pulsations may also be smeared out if the range of emitting radii is large and the Lorentz factor of the wind is low (§3).

The second, much stronger HE gamma-ray detection of PSR B1259-63 that occurred about a month after periastron passage is not explained in this model without additional assumptions. One possibility is additional seed photons provided by the PWN: in this case, the peak contribution arises after periastron when the PWN is in between the observer and the pulsar, a favorable configuration for inverse Compton scattering (§4.1). We note that a similar shift in phase of peak HE gamma-ray emission is observed in LS I +61°303 and could be explained similarly.

Emission from a striped pulsar wind might solve the puzzle of the pulsar-like HE gamma-ray spectrum with a flux modulated on the orbital period in the gamma-ray binaries LS 5039 and LS I +61°303. The HE emission is stronger than in PSR B1259-63 because of the higher stellar photon densities. Significant HE gamma-ray emission requires that the stripes are oriented towards us. Systems where this is not the case could still be detected through their radio, X-ray or VHE emission (attributed to the PWN) but will not display strong HE emission. One such system might be HESS J0632+057 (§4.2).

Gamma-ray binaries may thus be providing indirect evidence for striped wind emission. If verified by the detection of pulsations in HE gamma rays, this would bolster the view that pulsar HE emission originates beyond the light cylinder.

## ACKNOWLEDGMENTS

We thank D. Khangulyan and V. Bosch-Ramon for pointing out an error in the first draft of this paper, B. Cerutti and G. Henri for helpful discussions. This work was supported by the European Community via contract ERC-StG-200911.

## REFERENCES

- Abdo, A. A., Ackermann, M., Ajello, M., et al. 2010a, *ApJS*, 187, 460
- Abdo, A. A., Ackermann, M., Ajello, M., et al. 2009a, *ApJL*, 701, L123
- Abdo, A. A., Ackermann, M., Ajello, M., et al. 2009b, *ApJL*, 706, L56
- Abdo, A. A., Fermi LAT Collaboration, Chernyakova, M., et al. 2011a, *ArXiv e-prints* 1103.4108
- Abdo, A. A., Parent, D., Dubois, R., & Roberts, M. 2011b, *The Astronomer's Telegram*, 3115, 1
- Abdo, A. A., Parent, D., Grove, J. E., et al. 2010b, *The Astronomer's Telegram*, 3085, 1
- Aharonian, F., Akhperjanian, A. G., Anton, G., et al. 2009, *A&A*, 507, 389
- Aharonian, F., Akhperjanian, A. G., Aye, K., et al. 2005, *A&A*, 442, 1
- Bai, X. & Spitkovsky, A. 2010, *ApJ*, 715, 1282
- Ball, L. & Kirk, J. G. 2000, *Astroparticle Physics*, 12, 335
- Bogovalov, S. V., Khangulyan, D. V., Koldoba, A. V., Ustyugova, G. V., & Aharonian, F. A. 2008, *MNRAS*, 387, 63
- Bogovalov, S. V. 1999, *A&A*, 349, 1017
- Cerutti, B., Dubus, G., & Henri, G. 2008, *A&A*, 488, 37
- Cheng, K. S. 2009, in *Astrophysics and Space Science Library*, Vol. 357, *Astrophysics and Space Science Library*, ed. W. Becker, 481–+
- Chernyakova, M., Neronov, A., Lutovinov, A., Rodriguez, J., & Johnston, S. 2006, *MNRAS*, 367, 1201
- Connors, T. W., Johnston, S., Manchester, R. N., & McConnell, D. 2002, *MNRAS*, 336, 1201
- Coroniti, F. V. 1990, *ApJ*, 349, 538
- Dubus, G. 2006, *A&A*, 456, 801
- Dubus, G., Cerutti, B., & Henri, G. 2008, *A&A*, 477, 691
- Dubus, G., Cerutti, B., & Henri, G. 2010, *A&A*, 516, A18+
- Harding, A. K. 2009, in *Astrophysics and Space Science Library*, Vol. 357, *Astrophysics and Space Science Library*, ed. W. Becker, 521–+
- Hinton, J. A., Skilton, J. L., Funk, S., et al. 2009, *ApJL*, 690, L101
- Johnston, S., Manchester, R. N., Lyne, A. G., Nicastro, L., & Spyromilio, J. 1994, *MNRAS*, 268, 430
- Khangulyan, D., Hnatic, S., Aharonian, F., & Bogovalov, S. 2007, *MNRAS*, 380, 320
- Kirk, J. G., Skjæraasen, O., & Gallant, Y. A. 2002, *A&A*, 388, L29
- Kong, A. K. H., Huang, R. H. H., Tam, P. H. T., & Hui, C. Y. 2011, *The Astronomer's Telegram*, 3111, 1
- Lyubarsky, Y. & Kirk, J. G. 2001, *ApJ*, 547, 437
- Melatos, A., Johnston, S., & Melrose, D. B. 1995, *MNRAS*, 275, 381
- Michel, F. C. 1994, *ApJ*, 431, 397
- Moskalenko, I. V. & Strong, A. W. 2000, *ApJ*, 528, 357
- Negueruela, I., Ribó, M., Herrero, A., Lorenzo, J., Khangulyan, D., & Aharonian, F. A. 2011, *arXiv:1103.4636*
- Pétri, J. 2008, in *SF2A-2008*, ed. C. Charbonnel, F. Combes, & R. Samadi, 259–+
- Pétri, J. 2009, *A&A*, 503, 13
- Pétri, J. 2011, *MNRAS*, 412, 1870
- Pétri, J. & Kirk, J. G. 2005, *ApJL*, 627, L37
- Pétri, J. & Lyubarsky, Y. 2007, *A&A*, 473, 683
- Sierpowska, A. & Bednarek, W. 2005, *MNRAS*, 356, 711
- Sierpowska-Bartosik, A. & Torres, D. F. 2007, *ApJL*, 671, L145
- Sierpowska-Bartosik, A. & Torres, D. F. 2008, *Astroparticle Physics*, 30, 239
- Stairs, I. H., Lyne, A. G., & Shemar, S. L. 2000, *Nature*, 406, 484
- Tam, P. H. T., Huang, R. H. H., Takata, J., et al. 2011, *ArXiv e-prints* 1103.3129
- Tavani, M., & Arons, J. 1997, *ApJ*, 477, 439
- van Soelen, B., & Meintjes, P. J. 2011, *MNRAS*, 17
- Wang, N., Johnston, S., & Manchester, R. N. 2004, *MNRAS*, 351, 599

## APPENDIX A: ANISOTROPIC INVERSE COMPTON EMISSION FROM A POWER-LAW DISTRIBUTION OF ELECTRONS

In this appendix, we give some details about the analytical expressions used to compute the spectrum arising from anisotropic Inverse Compton scattering by a power-law distribution of high energy leptons with index  $p$  (Eq. (1)).

The scattering rate for an anisotropic and mono-energetic target photon field with  $\vec{n}$  the direction of propagation of these incoming photons and  $\varepsilon_1$  their energy, normalized to the electron rest mass energy  $m_e c^2$ , is given according to Moskalenko & Strong (2000) by

$$\frac{dN}{dt d\varepsilon_2}(\gamma, \varepsilon_1, \varepsilon_2, \zeta) = \frac{3}{8} \frac{\sigma_T c}{\varepsilon_1 (\gamma - \varepsilon_2)^2} \left[ 2 - 2 \frac{\varepsilon_2}{\gamma} \left( \frac{1}{\varepsilon_1'} + 2 \right) + \frac{\varepsilon_2^2}{\gamma^2} \left( \frac{1}{\varepsilon_1'^2} + \frac{2}{\varepsilon_1'} + 3 \right) - \frac{\varepsilon_2^3}{\gamma^3} \right] \quad (\text{A1})$$

$$\varepsilon_1' = \gamma \varepsilon_1 (1 - \beta \cdot \mathbf{n}) \quad (\text{A2})$$

$$= \gamma \varepsilon_1 (1 + \beta \cos \zeta) \quad (\text{A3})$$

$$\varepsilon_2 \leq \frac{2\gamma \varepsilon_1'}{1 + 2\varepsilon_1'} < \gamma \quad (\text{A4})$$

where  $\gamma$  is the Lorentz factor of the electron,  $\vec{\beta}$  its 3-velocity,  $\zeta$  the angle between photon direction and lepton velocity ( $\zeta = 0$  for head-on collision) and  $\varepsilon_2$  the up-scattered photon energy (also normalized to the electron rest mass energy). All useful quantities are measured in the observer frame except for  $\varepsilon_1'$  which represents the incoming photon normalized energy as measured in the electron rest frame. We checked that this formula gives identical results to Eq. (A.5) of Dubus et al. (2008) in the ultra-relativistic limit  $\gamma \gg 1$ . In this limit,  $\frac{dN}{dt d\varepsilon_2}$  is a polynomial in  $1/\gamma$ . Integration over the particle distribution (i.e. over  $\gamma$ ) can be performed analytically when the distribution is a power-law with an integer or half-integer spectral index  $p$ .

The spectrum is given by

$$\frac{dI}{dt d\varepsilon_2}(\varepsilon_1, \varepsilon_2, \zeta) = K_e \varepsilon_2 \int_{\gamma_1}^{\gamma_2} \frac{dN}{dt d\varepsilon_2} \gamma^{-p} d\gamma \quad (\text{A5})$$

with

$$\gamma_1 = \text{Max} \left( \frac{\varepsilon_2}{2} \left[ 1 + \sqrt{1 + \frac{2}{\varepsilon_1 \varepsilon_2 (1 + \cos \zeta)}} \right], \gamma_{\min} \right) \quad (\text{A6})$$

$$\gamma_2 = \text{Max} \left( \frac{\varepsilon_2}{2} \left[ 1 + \sqrt{1 + \frac{2}{\varepsilon_1 \varepsilon_2 (1 + \cos \zeta)}} \right], \gamma_{\max} \right) \quad (\text{A7})$$

In the case  $p = 2$  used in our work, we find

$$\int_{\gamma_1}^{\gamma_2} \frac{dN}{dt d\varepsilon_2} \gamma^{-2} d\gamma = \frac{1}{1280 \gamma^5 \pi \varepsilon_1^3 (\gamma - \varepsilon_2) \varepsilon_2^5} \times$$

$$(3 (60(\gamma - \varepsilon_2)(\log(\gamma) - \log(\gamma - \varepsilon_2))\gamma^5 + \varepsilon_2 (-60\gamma^5 + 30\varepsilon_2\gamma^4 + 10\varepsilon_2^2\gamma^3 + 5\varepsilon_2^3\gamma^2 + 3\varepsilon_2^4\gamma + 2\varepsilon_2^5)) \sec^4 \left( \frac{\zeta}{2} \right) +$$

$$10\gamma\varepsilon_1\varepsilon_2(\varepsilon_2 - \gamma) (12(\log(\gamma - \varepsilon_2) - \log(\gamma))\gamma^4 + \varepsilon_2 (12\gamma^3 + 6\varepsilon_2\gamma^2 + 4\varepsilon_2^2\gamma + 3\varepsilon_2^3)) \sec^2 \left( \frac{\zeta}{2} \right) -$$

$$10\gamma\varepsilon_1^2\varepsilon_2^2(\varepsilon_2 - \gamma) (12(\log(\gamma - \varepsilon_2) - \log(\gamma))\gamma^4 + \varepsilon_2 (12\gamma^3 + 6\varepsilon_2\gamma^2 - 4\varepsilon_2^2\gamma + 3\varepsilon_2^3))) \Big|_{\gamma_1}^{\gamma_2} \quad (\text{A8})$$